SANDIA REPORT
SAND 2004-1739
Unlimited Release
Printed May 2004

Helium Nano-Bubble Evolution in Aging Metal Tritides

Donald F. Cowgill

Prepared by
Sandia National Laboratories
Albuquerque, New Mexico 87185 and Livermore, California 94550

Sandia is a multiprogram laboratory operated by Sandia Corporation,
a Lockheed Martin Company, for the United States Department of Energy's
National Nuclear Security Administration under Contract DE-AC04-94AL85000.

Sandia National Laboratories

TOTAL PAGES: 42

Issued by Sandia National Laboratories, operated for the United States Department of Energy by Sandia Corporation.

Available to DOE and DOE contractors from
U.S. Department of Energy
Office of Scientific and Technical Information
P.O. Box 62
Oak Ridge, TN 37831

Telephone: (865)576-8401
Facsimile: (865)576-5728
E-Mail: reports@adonis.osti.gov
Online ordering: http://www.doe.gov/bridge

Available to the public from
U.S. Department of Commerce
National Technical Information Service
5285 Port Royal Rd
Springfield, VA 22161

Telephone: (800)553-6847
Facsimile: (703)605-6900
E-Mail: orders@ntis.fedworld.gov
Online order: http://www.ntis.gov/help/ordermethods.asp?loc=7-4-0#online

SAND 2004-1739
Unlimited Release
Printed May 2004

Helium Nano-Bubble Evolution in Aging Metal Tritides

Donald F. Cowgill
Materials and Engineering Sciences Center
Sandia National Laboratories
P.O. Box 969
Livermore, CA 94551-9402

Abstract

A continuum-scale, evolutionary model of helium (He) nano-bubble nucleation, growth and He release for aging bulk metal tritides is presented which accounts for major features of the experimental database. Bubble nucleation, modeled as self-trapping of interstitially diffusing He atoms, is found to occur during the first few days following tritium introduction into the metal and is sensitive to the He diffusivity and pairing energy. An effective helium diffusivity of 0.3×10^{-16} cm^2/s at 300 K is required to generate the average bubble density of 5×10^{17} bubbles/cm^3 observed by transmission electron microscopy (TEM). Early bubble growth by dislocation loop punching with a 1/radius bubble pressure dependence produces good agreement with He atomic volumes and bubble pressures determined from swelling data, nuclear magnetic resonance (NMR) measurements, and hydride pressure-composition-temperature (PCT) shifts. The model predicts that later in life neighboring bubble interactions may first lower the loop punching pressure through cooperative stress effects, then raise the pressure by partial blocking of loops. It also accounts for the shape of the bubble spacing distribution obtained from NMR data. This distribution is found to remain fixed with age, justifying the separation of nucleation and growth phases, providing a sensitive test of the growth formulation, and indicating that further significant bubble nucleation does not occur throughout life. Helium generated within the escape depth of surfaces and surface-connected porosity produces the low-level early helium release. Accelerated or rapid release is modeled as inter-bubble fracture using an average ligament stress criterion. Good agreement is found between the predicted onset of fracture and the observed He/Metal ratio (He/M) for rapid He release from bulk palladium tritide. An examination of how inter-bubble fracture varies over the bubble spacing distribution shows that the critical He/M will be lower for thin films or small particle material. It is concluded that control of He retention can be accomplished through control of bubble nucleation.

ACKNOWLEGEMENTS

The author wishes to acknowledge valuable discussions regarding the development of this model with K.L. Wilson, J.A. Zimmerman, W.G. Wolfer, C. Krenn, G.J. Thomas, R.A Causey, K.L. Hertz, and S.L. Robinson. Special thanks are given to G.C. Story for his strong support and encouragement regarding this effort.

Contents

Figures

Tables

INTRODUCTION

High-resolution TEM [1-3], NMR [4-6] measurements, and theoretical studies [7-9] have shown that helium generated in aging bulk metal tritides is retained in high-pressure nano-bubbles. Helium is created by tritium decay with insufficient energy to displace the metal host atoms and generate trapping sites. The He atoms occupy interstitial sites and are mobile [10-13] at room temperature. They produce distortion of the metal lattice, which in turn causes them to cluster in the local expansion produced by neighbors. When the clusters reach a critical size (5-6 He), they force the ejection of a metal atom, forming the nucleus of a stable He bubble [7]. This paper models the three stages of bubble evolution in bulk material: bubble nucleation, bubble growth, and helium release.

Helium bubbles are nucleated by the self-trapping mechanism described above or by trapping at enlarged sites near impurities and structural defects in the host lattice. The latter process (heterogeneous nucleation) depends on the material's intrinsic microstructure and can be treated by superposition on the homogeneous behavior. It can be important, for example, for metal tritide films containing high concentrations of dislocations, but is not considered here. Homogeneous nucleation occurs rapidly, beginning as soon as the mobile He/Metal concentration (He/M) reaches a few atomic parts per million (appm), then decreases when the concentration of bubble surface sites becomes sufficient to provide sinks for newly-generated He. Thereafter, each bubble's growth is determined by its He supply rate, i.e., the He source volume for the bubble, and by the mechanical strength of the lattice. The mechanism for rapid or "accelerated" He release at room temperature remains uncertain. This release may result from inter-bubble fracture of the metal ligaments between bubbles or by inter-bubble He migration between adjacent bubbles in the strained (expanded) lattice. Rapid He release will occur when this fracture or migration network becomes sufficiently interconnected. Bubble migration and coarsening, which occur at higher temperatures, are beyond the scope of this paper.

The model begins by describing the bubble nucleation stage using a set of rate equations. Here, effective He migration parameters are deduced by comparing the computed bubble density with that found by high resolution transmission electron microscopy (TEM). Next, the growth stage is examined and the model is tested using ^{3}He nuclear magnetic resonance (NMR), material swelling, and metal hydride pressure-composition-temperature (PCT) data. The palladium tritide system is used for these comparisons, as it has the most extensive experimental database available. Here, comparison of the bubble source volume distribution (bubble spacing distribution) at various ages, deduced from the NMR data, shows that latent bubble nucleation is indeed negligible and justifies separation of the nucleation and growth stages. As bubble-bubble interactions become large, neighbor stress-assisted growth is proposed to occur, potentially leading to anisotropic bubble growth and bubble ordering along Burgers vectors. Finally, He release is modeled as diffusive release (early release) for He generated near surfaces and as inter-bubble fracture (rapid release) using an average ligament stress criterion. The onset of rapid release from bulk material is proposed to occur when the ligaments between bubbles at the mean bubble density undergo inter-bubble fracture.

While developed specifically for helium in metals, the model has general applicability to a wide range of problems involving mobile species injected into materials where local concentrations exceed the solubility limit. It provides a framework for following the evolution of the resulting precipitates. Throughout, an effort has been made to capture the essential physics without adding unnecessary detail. Complex expressions adding small corrections to the physical processes are used only when warranted by the experimental database. It is concluded from the model presented here that control of He retention within aging tritides requires control of bubble nucleation. It is also concluded that sensitive testing and validation of the model will require additional measurements on the He bubbles themselves.

BUBBLE NUCLEATION

Bubble nucleation in the absence of intrinsic trapping defects is determined by the probability of two He atoms finding each other while diffusing interstitially through the metal tritide lattice. According to the self-trapping energetics of Wilson *et al.* [7], He atoms clustered in adjacent interstitial sites may dissociate (detrap) until the cluster reaches a critical size of N=5 or 6 atoms, where upon they eject a metal atom and form a stable "bubble". The rate equation for each of the N (He atom) species has generation and loss terms. N-species are generated by promotion from (N-1)-species and by dissociation of (N+1)-species. Loss of N-species occurs by promotion to (N+1)-species and by self-dissociation. The differential equations containing these respective terms for the N-species concentration c_N, per metal atom, are:

$$dc_N/dt = p_1 s_{N-1} c_1 c_{N-1} + q_{N+1} c_{N+1} - p_1 s_N c_1 c_N - q_N c_N, \quad (1)$$

for N>1. Here p_1 is the atomic He hop rate (jumps/s) between interstitial sites, s_N is the number of trapping sites around an N-species, and q_N is the N-species dissociation rate. For small N, each of the N atoms can cause dissociation and thus q_N is proportional to $[N \exp(-E_N/kT)]$. The self-trapping calculations in several fcc metals found that the binding energy for N=3 triplets, E_3, is about 3 times larger than for pairs, E_2, and increases further with increasing N. Thus during the nucleation stage, when $c_{N+1} \leq c_N$, triplet and higher-order cluster dissociation is relatively unimportant and one may regard $N \geq 3$ as a stable nucleus.

The coupled differential equations for the nucleation kinetics which follow the mobile He concentration c_1 (mobile He/M), pair concentration c_2 (pairs/M), and stable bubble concentration c_B (bubbles/M) are:

$$dc_1/dt = g - 2p_1 s_1 c_1^2 + 2q_2 c_2 - p_1 s_2 c_1 c_2 - p_1 s_B c_1 c_B \quad (2)$$

$$dc_2/dt = p_1 s_1 c_1^2 - p_1 s_2 c_1 c_2 - q_2 c_2 \quad (3)$$

$$dc_B/dt = p_1 s_2 c_1 c_2. \quad (4)$$

Here $g=\lambda(^3H/M)$ is the atomic He generation rate ($\lambda=1.79\times10^{-9}$ s^{-1}, the tritium ^3H decay constant); q_2 is the pair dissociation rate; and s_1, s_2, $s_B(r)$ are the number of trapping sites associated with a He atom, pair, and bubble of radius r. Even for a tritide with a decaying tritium concentration, where $^3H(t)=^3H(0)\exp(-\lambda t)$, g may be considered constant during the relatively the short bubble nucleation stage.

Atomic helium generated within an fcc tritide structure diffuses among the 12 adjacent octahedral lattice sites. Thus the hop rate is $p_1=12D/b^2$, where D is the interstitial diffusion coefficient and $b=a_o/2^{1/2}$ is the hop distance in a lattice with parameter a_o. Helium pairing reduces this mobility by the trapping factor $\exp(-E_2/kT)$, giving a corresponding pair dissociation rate $q_2=2p_1(7/12)\exp(-E_2/kT)$. Here the factor (7/12) accounts for the fraction of adjacent sites which will cause dissociation for either of the 2 He atoms. The number of trap

sites associated with an interstitial He atom is s_1=12, He-pair is s_2=19, and He-triplet is s_3=23. The effective number of sites surrounding a bubble of radius r is taken to be the number surface sites $s_B(r)=4\pi(r+a/2)^2 n_{mh}^{2/3}$, where n_{mh} is the metal atom density in the metal hydride phase. Here, an average distance from the bubble surface to nearest octahedral site $a/2=(1/2)(a_o/2+b/2)$ is added to the bubble radius give the effective radius $r'=r+a/2$ of the trapping surface. The bubble radius is in turn determined by $Nv_a=(4/3)\pi r^3$, where v_a is the effective He atomic volume within the bubble. Early swelling data on numerous tritides shows v_a to be nearly constant for very small bubbles. This is examined in detail in the section on Bubble Growth.

Bubble Nucleation in Palladium Tritide

Numerical integration of Eqs. (2)-(4) results in the nucleation pulse behavior shown in Figure 1 for $PdT_{0.6}$ at 300 K. Here, the pair and triplet binding energies were taken from theory [14] to be E_2=0.13 eV and E_3=.40 eV, respectively. The mobile concentration c_1 rises rapidly, then drops as the growing concentration of bubbles c_B provides additional trapping sites. The pair concentration (not shown) closely follows the mobile concentration. Ninety percent of the bubbles are nucleated within 3 days. The amplitude and duration of the mobile pulse depends primarily on competition between the generation rate g and hop rate p_1.

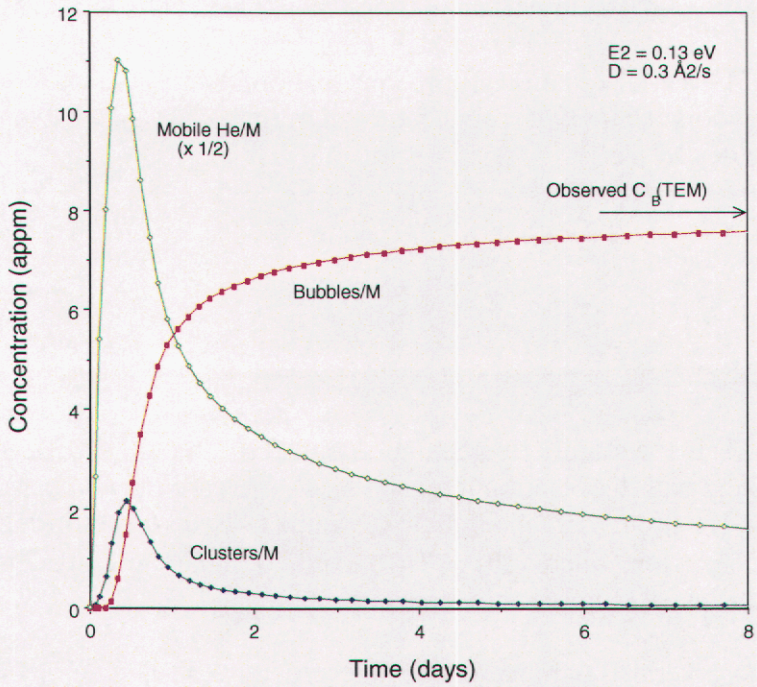

Figure 1. Computed bubble nucleation pulse in palladium tritide at 300 K showing concentrations of mobile He (N=1), clusters (2≤N≤5), and "stable bubbles" (N≥3). The asymptotic value of c_B is matched to the bubble density observed by TEM [1] by adjusting the He diffusivity D.

Decreasing the He diffusivity or increasing the generation rate (e.g., by increasing the ^{3}H concentration) increases the bubble density. For the calculation shown here, the diffusivity was ajusted to produce a saturation bubble density in agreement with the value $5x10^{17}$ bubbles/cm^3 (c_B=$8x10^{-6}$ bubbles/M) found by TEM [1] for $PdT_{0.6}$. This fit requires a He diffusivity of D=$0.3x10^{-16}$ cm^2/s. We have recently measured the effective He diffusivity in several materials near room temperature using a low-energy He implantation / re-emission technique and found it in the range 0.2-$2x10^{-16}$ cm^2/s with activation energy of 0.15-0.3 eV [15]. Other measurements of the He diffusivity (and diffusion barrier) extrapolated to 300 K vary widely, from 10^{-20} cm^2/s (1 eV) and 10^{-14} cm^2/s (.62 eV) in hcp Ti and Mg [16], respectively; to 10^{-9} cm^2/s (.35 eV) in fcc Ni [10]; to even higher values of 10^{-8} cm^2/s (1 eV) and 10^{-7} cm^2/s (.28 eV) in bcc Cu [12] and W [17], respectively.

The ultimate bubble density depends only weakly on the pairing energy E_2, which accounts for the similarity of bubble densities observed in a number of fcc tritides [1-3, 18-20]. For example, increasing E_2 to 0.22 eV, the theoretical value for Ni [7], would need a diffusivity of $1.8x10^{-16}$ cm^2/s to generate the observed c_B. An examination of the sensitivity of c_B to the nucleation parameters shows that individually increasing E_2 to 0.22 eV, increases c_B by 23%; while bubble nucleation in a di-tritide with ^{3}H/M=2 increases c_B by 2x. The nucleation calculation of Figure 1 was done for ^{3}H/Pd=0.60 for direct comparison with the TEM data on samples prepared at that stoichiometry. The bubble growth calculations given in the next section are performed for ^{3}H/Pd=0.67 in order to make use of the available mechanical property data. Bubble nucleation at this slightly higher stoichiometry increases the mean bubble density by about 6%, assuming the same diffusion and trapping parameters, much less than the uncertainty of the experimental data sets used in the comparisons.

Adding a separate differential equation for triplets c_3, along with terms for their dissociation, produces no resolvable change in c_1, c_2, or c_B. This verifies that the infrequent dissociation of triplets with $E_3 \geq 0.4$ eV is indeed inconsequential to the nucleation process. Since the nucleation ends long before the bubbles experience significant growth, it is also insensitive to the number of trap sites per bubble $s_B(r)$ for larger bubbles; i.e., for N>30. The results are, however, somewhat sensitive to the number of sites surrounding the growing He clusters and very small bubbles during the early stages. For the He clustering stage, these values were taken to be s_1=12, s_2=19, s_3=23, s_4=27, s_5=31, then continuing to increase more slowly according to the bubble's spherical surface with v_a=8.8 Å^3, as determined from early swelling behavior. (See section on Bubble Growth). These site numbers were estimated by considering probable clustering geometries according to Wilson *et al.* [14].

Expanding the set of differential equations to specifically follow c_1 through c_5, along with c_B allows examination of the concentration of clusters $c_C = c_2+c_3+c_4+c_5$ prior to metal atom displacement. This cluster concentration is also shown in Figure 1. The He clustering pulse occurs simultaneously with the mobile He pulse and causes only a slight (10 hr) delay in the rise of $c_{N>5}$. At this point, the total He/M concentration is about 40 appm. Beyond this point, the He clusters (and their effects on lattice distortion through a high occupancy of O-sites) no longer occur.

ISOLATED BUBBLE GROWTH

Following nucleation, each bubble grows according to the helium source volume surrounding the bubble. This volume is defined by the surface between bubbles where the He flux is zero; i.e., where the influx equals the outflux. For uniform bubble spacing, this surface is midway between adjacent bubbles and the array of source volumes can be described by a packing of spherical volumes of radius R. (See inset sketch in Figure 2b.) After nucleation has completed, this may be regarded to be a fixed packing in time. For n_B bubbles/cm^3, the entire volume is included by writing:

$$(4/3)\pi R^3 n_B = f_p, \tag{5}$$

where f_p is a packing fraction added to account for contributions from the additional source volume between touching spheres. This packing fraction has been calculated [21] for various sphere array geometries. It varies from f_p=0.74 for tight fcc or hcp packing to f_p=0.34 for loose tetrahedral packing. For a random bubble array, Wolfer [22] gives f_p=0.64.

It is assumed here that the metal atoms displaced during bubble growth remain within the bubble's source volume. On average, for bulk materials, any metal flux out of R equals the flux into R from neighboring bubble growth, giving a net zero metal atom flux. Under this condition, R^3-r^3 is constant, where r is the bubble radius. This requires R to slowly increase (and n_B to slowly decrease) as the bubbles grow. This assumption may not be true, at least initially, for bubbles in small grain thin films or in small particle powders, where the ejected atoms can leave the source volume and build up on the grain surface. However, the large bubbles occurring later in life likely limit such transport over long distances. For the calculations given below, it will be assumed that the effective tritide volume $(4/3)\pi(R^3-r^3)$ contributing to a bubble remains constant with time.

If the tritium concentration (^{3}H/M) also remains homogeneous, the bubbles grow according to their distribution of source volumes. The number of He atoms per bubble N is given by:

$$N = [(4/3)\pi(R^3-r^3)/f_p]\, n_{mh}\, (He/M). \tag{6}$$

The He/M atom ratio increases according to the tritium decay constant λ=1.79x10^{-9} s^{-1}; i.e., He/M=(^{3}H/M)$_0$ [1-e$^{-\lambda t}$] for a fixed quantity of tritium, or He/M=(^{3}H/M)λt in a tritium overpressure where ^{3}H/M is kept constant. The number of helium atoms per bubble is also given by $N=(4/3)\pi r^3/v_a$, the bubble volume divided by the He atomic volume v_a within the bubble. Combining these gives a simple expression relating the He/M concentration to (r/R'), the ratio of the bubble radius r to its effective source radius $R'=(R^3-r^3)^{1/3}$,

$$He/M = (f_p/n_{mh}v_a)\,(r/R')^3. \tag{7}$$

For the small, well-separated bubbles occurring early in life, $R'=R[1-(r/R)^3]^{1/3}\approx R$.

At room temperature, the bubbles in many tritides, including palladium tritide, are believed to grow by dislocation loop punching [9, 23]. For isolated bubbles larger than a few metal atom spacings, Trinkaus [24] relates the bubble pressure p to its radius r by:

$$p_{isol} = 2\gamma/r + \mu b/r, \tag{8}$$

where γ is the surface free energy, μ is the shear modulus of the lattice, and b is the Burgers vector (here, the nearest-neighbor distance between metal atoms). For large bubbles ($r \geq 4\pi b$), he argues [25] the second term may limit at $\mu/4\pi$ due to elastic interactions within the lattice. Other more complex expressions have been formulated by Greenwood *et al.* [23] and others [26], and compared by Donnelly [27]. It is found below that the simple 1/r dependence of Eq. (8) fits the available experimental data better than the more complicated expressions.

The He pressure p within a bubble is related to its atomic volume v_a by the He equation-of-state (EOS). Except for very small bubbles (very early in life), where wall curvature effects can become important [26], v_a is described by the bulk high pressure He EOS. Wolfer *et al.* [26] and Donnelly [27] examined various published He EOS and concluded that for the pressure and temperature range of interest, the best available He EOS is that of Mills *et al.* [28]:

$$v = (22.575 + .0064655T - 7.2645T^{-1/2})\, P^{-1/3} + (-12.483 - .024549T)\, P^{-2/3} + (1.0596 + .10604T - 19.641T^{-1/2} + 189.84T^{-1})\, P^{-1}, \tag{9}$$

where $v(cm^3/mole)$, P(kbar), T(K). At T=300 K this equation becomes:

$$v_a = 18.572\, p^{-1/3} - 7.101\, p^{-2/3} + 5.375\, p^{-1}, \tag{10}$$

for atomic volume $v_a(\text{Å}^3)$ and helium pressure p(GPa). A good fit to the inverted form of Eq. (10) over the range $5 < v_a < 20$ Å^3 is given by:

$$1/p = .1196 - .04801\, v_a + .005955\, v_a^2. \tag{11}$$

Isolated Bubble Growth in Palladium Tritide

A simple method for evaluating bubble growth r(He/M) using these equations, given an initial bubble spacing R (or spacing distribution), is to begin with a bubble radius r and evaluate r/R, then p using Eq. (8), then v_a using Eq. (10), and finally He/M using Eq. (7). Aside from the material properties, the only adjustable parameter in this calculation is the bubble density n_B, or equivalently, the He source radius R, related by Eq. (5). The relevant material properties are listed in Table I. The surface energy was obtained from the surface tension of liquid Pd [29] and corrected [27] for the volume change from the melting temperature T_M to room temperature with $\gamma(T_M)/\gamma(RT) = (V_M/V_{RT})^{2/3}$, using high temperature thermal expansion data for Pd [30]. Mechanical properties of palladium hydride are available for the stoichiometry H/Pd=0.67; thus the evaluations of bubble growth are done for $PdT_{0.67}$. The shear modulus for dislocation loop punching in the (110) direction, which

occurs via a jog through (112), $\mu=G_{112}^{R}$, was calculated from single crystal elastic constants C_{ij} for the metal [31] and hydride phases [32] using the expression for the "relaxed modulus" [33], $G_{112}^{R}=3C_{44}(C_{11}-C_{12})/(4C_{44}+C_{11}-C_{12})$. The theoretical fracture strength σ_F, used for inter-bubble fracture in the next section, was taken as $(4/3)\tau_{max}$, where $\tau_{max}=2.1$ GPa is the hydride's ideal strength as calculated by Krenn [34]. Evaluations are also made using the somewhat higher fracture strength $G/4\pi$, where G is the shear modulus [35] deduced from elastic constants using the average of the Voigt and Reuss averaging methods (V-R) for polycrystalline material. For the $PdT_{.67}$ fcc structure, $v_{mh}=1/n_{mh}=16.4$ Å^3 and $b=a_0\sqrt{2}$, where $a_0=4.033$ Å is the lattice parameter [36].

Table I. Mechanical properties of Pd and Pd hydride used in the bubble growth and fracture calculations.

Parameter		H/M	Value	Source
Metal Density,	n_m	0	.06790 Å^{-3}	[36]
	n_{mh}	.67	.06098	[36]
Surface Energy,	$\gamma(T_M)$	0	14.7 GPa-Å	[29]
	γ(RT)	0	15.4	See text
Shear Modulus,	μ	0	32.3 GPa	G_{112}^{R}
	μ	.67	33.6	G_{112}^{R}
	G	0	47.2	V-R average
	G	.67	45.2	V-R average
Fracture Strength,	σ_F	0	3.54 GPa	$(4/3)\tau_{max}$
	σ_F	.67	2.80	$(4/3)\tau_{max}$
	σ_F	0	3.76	$G/4\pi$
	σ_F	.67	3.60	$G/4\pi$

Figure 2 shows the isolated bubble growth behavior computed using three initial bubble densities (n_B=2, 5, and 10 x10^{17} bubbles/cm^3) and a random bubble geometry. Here the bubble pressure was assumed described by Eq. (8), i.e., proportional to 1/r for all r. In Figure 2a, it is apparent that the more closely spaced bubbles are smaller at each age, as expected. However, when normalized by their respective source radii (Figure 2b), the three curves are nearly coincident. The small remaining difference results from lower pressures, and larger He atomic volumes, which occur in the larger bubbles at lower bubble density.

The effective He atomic volume and its increase with age is reflected in the bulk material swelling, which results primarily from the total volume occupied by the bubbles. The tritide swells with age, due to the combined linear increase in the number of He per bubble, with He/M, and the slow increase in v_a with increasing bubble size:

$$\Delta V/V = (v_a/v_{mh})(He/M). \qquad (12)$$

It is compared with the observed swelling in Figure 3. The experimental data at low He/M are from bulk length change measurements [37] and at higher He/M are from NMR determination of v_a obtained by observation of the liquid-solid He transition [5-6] within the

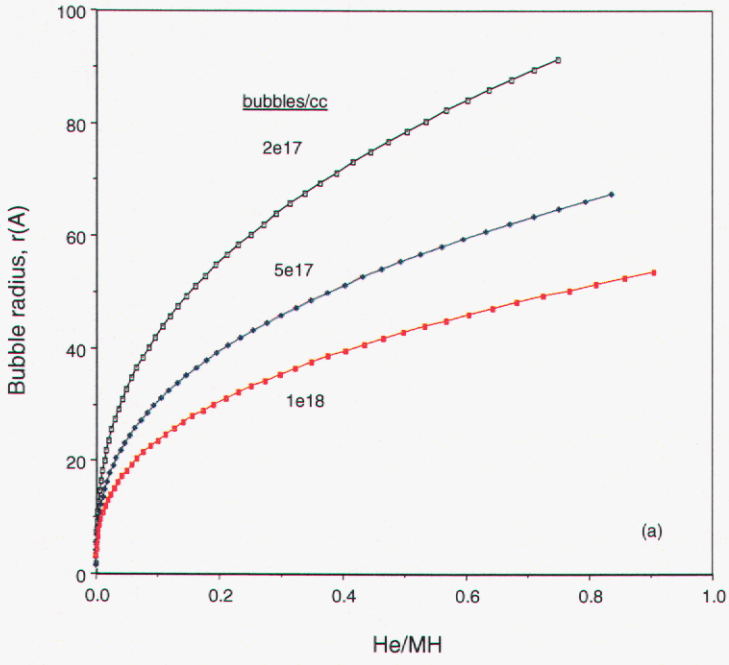

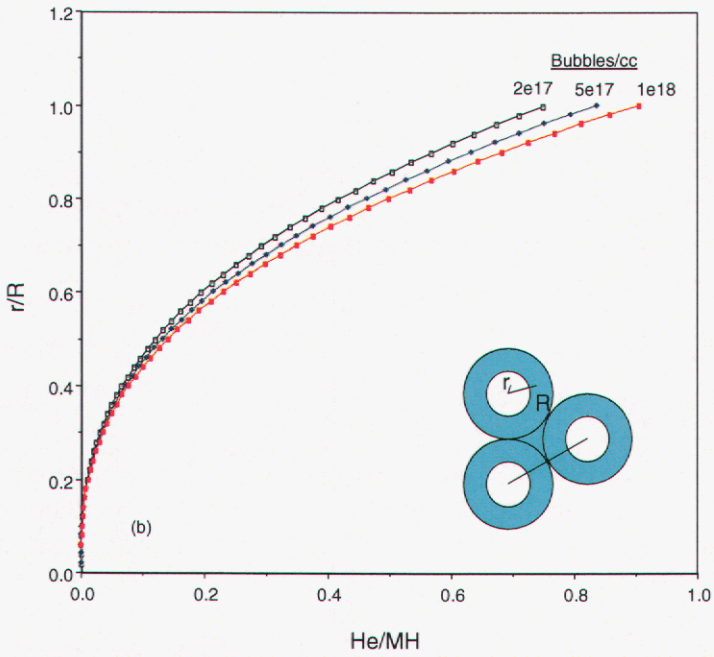

Figure 2. Computed isolated growth of (a) bubble radius and (b) bubble radius/spacing ratio with age in Pd tritide at three bubble densities.

bubbles at low temperatures. (Details of the NMR data analysis are given later in this paper.) Also shown is a single, rather uncertain, measurement on porous material using PVT techniques [38]. The important point here is that the swelling curve calculated for $n_B=5x10^{17}$ bubbles/cm^3 accurately fits the swelling data. Recall that this is the same bubble density

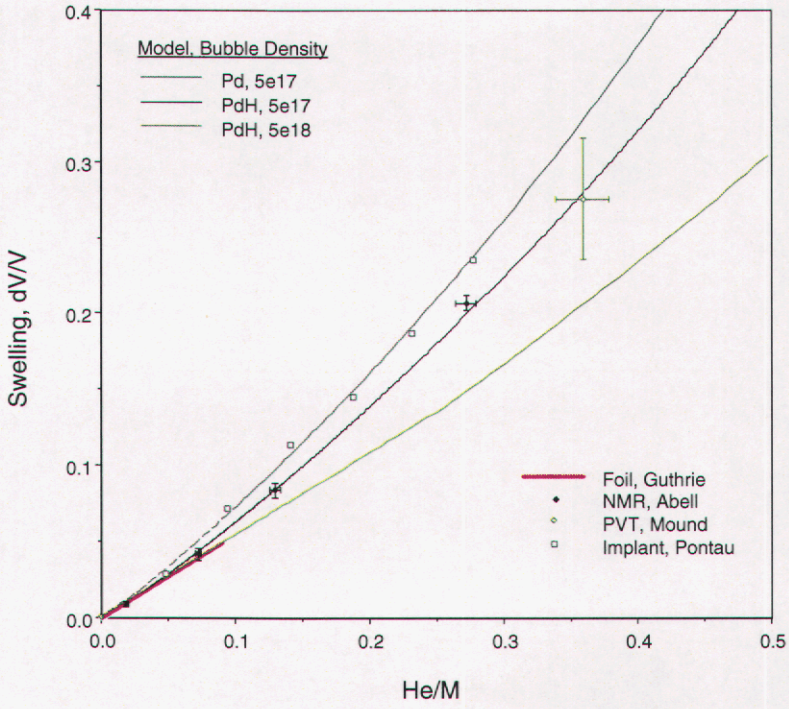

Figure 3. Bulk material swelling with increasing He/M. The swelling computed with 5x10^{17} bubbles/cm^3 fits data for both aging Pd tritide and He-implanted Pd. Swelling of the metal differs slightly from the hydride due differences in material parameters.

found by TEM [1] for aged $PdT_{0.6}$. Increasing the bubble density to $5x10^{18}$ bubbles/cm^3, as reported by Thiebaut *et al.* [39], reduces the computed swelling by 25%, well below the experimental observations, as indicated by the lower, dotted curve. Interestingly, data for He-implanted Pd foils [40] appear to fit the model using the same bubble density used for aged material. Here the slightly higher computed swelling results from the use of Pd, rather than $PdH_{0.67}$ parameters.

A limiting value of v_a for very small bubbles can be deduced from the slope of the swelling curve at early age. The early foil data of Guthrie [37] are described by $v_a/v_{mh}=0.54$, which gives the initial value $v_a=8.8$ Å^3. This value is used in the bubble nucleation calculation to determine the bubble surface area effective in trapping mobile He atoms and

terminating the nucleation pulse. The average value obtained by including the data at higher He/M concentration is v_a/v_{mh}=0.68, giving v_a=11.1 Å^3. These v_a are compared with values of the early v_a obtained by Schober *et al.* [41-44] for other tritides in Table II. These experimenters used precision dilatometry and other techniques to measure early swelling for

Table II. Swelling results from young metal tritides showing the narrow range of initial He atomic volume.

Material	Ref.	$(He/M)_{max}$	v_a/v_{mh}	v_a(Å^3)	p(GPa)	p/μ
$PdT_{.6}$	-	.08	.54	8.8	6.3	.19
$PdT_{.6}$	-	.30	.68	11.1	3.1	.09
$VT_{.02}$	[42]	.0006	.52	7.3	11.5	.25
$NbT_{.0253}$	[43]	.0019	.44	7.9±.3	9.0	.19
$NbT_{.59}$	[42]	.02	.39	7.7	9.7	.21
$TaT_{.0744}$	[43]	.0063	.39	7.1±.2	12.6	.20
$TaT_{.103}$	[41]	.0025	.53	10.0±.6	4.3	.07
$TaT_{.42}$	[41]	.004	.52	9.6±.6	4.8	.07
$TaT_{.37}$	[44]	.023	.38	7.2	12.1	.19
$LuT_{.13}$	[42]	.006	.23	6.8	14.6	.52
$LuT_{.15}$ (78 K)	[43]	.0069	.27	8.0±.5	8.6	.31
$LuT_{.11}$ (4 K)	[42]	.0004	.24	7.1	-	-

*After holding at 10 K for 10 days.

bulk samples with various concentrations of tritium, which decreased with time. After correcting for the change in metal tritide volume, they typically found linear expansion behavior, from which they deduced a constant He atomic volume. Their values typically fall around 7-8 Å^3. Using the bulk EOS to deduce an average bubble pressure gives a pressure around $\mu/2\pi$ or 0.2μ, as pointed out by Schober [43].

The linear swelling behavior at low He/M does not provide a sensitive test of the bubble growth model. It is only indicative of the buildup in He/M with time due to tritium decay. For defect-free materials with low tritium concentrations, the bubble densities will be low and bubbles should quickly reach a few nanometers diameter. Evaluation of the terms in Eq. (10) for bubbles of this size shows the first term dominates and thus v_a varies roughly as $p^{-1/3}$. Using Eq. (8) and $Nv_a=(4/3)\pi r^3$, one finds v_a is proportional to $N^{1/8}$. That is, for a given sample, an order of magnitude increase in the number of He per bubble will only produce a 30 percent change in v_a. Thus, small volume changes in bubbles of this size will produce very little effect on v_a. Inclusion of additional physics to describe this upper limit to bubble pressures for very small bubbles seems primarily of academic interest. Aside from its weak effect on bubble nucleation, the He atomic volume at early age appears to have little impact on the ultimate He retention behavior. A more sensitive test of the model is provided by the Pd NMR data, which extends over a significantly larger range in bubble size. In addition, NMR provides a determination of the He atomic volume independent of the quantity He in the material. For the larger bubbles in PdT, Table II shows that v_a increases significantly from the initial value.

THE BUBBLE SPACING DISTRIBUTION

The ^{3}He NMR experiments on aged PdT_x powders [5-6] provide more information than just the mean He density or pressure within the bubbles. They give measurements of the distribution of He atoms at each density (or pressure) as a function of age. The growth relations given above provide a one-to-one relationship between these He densities and the bubble radii r; and hence for each age or He/M, they give a unique distribution in bubble spacing R. It is instructive to evaluate this unique R-distribution from the NMR data set for each sample and then compare these R-distributions to determine the extent to which additional bubble nucleation occurred during the long term bubble growth.

Experimentally, each He distribution was obtained by setting the sample temperature and deducing the fraction of He in the liquid state $f_{liq}(T)$, then varying the temperature and re-measuring the liquid fraction. Abell and Attalla [5] showed that the abrupt change in He motion with change-of-state causes the NMR T_1 relaxation to follow the well-understood, temperature dependent BPP behavior [45] allowing the liquid He fraction to be quantitatively differentiated from the solid He. The helium atom density corresponding to this melting temperature is given by the bulk He melting curve [46]

$$1/v(cm^3/mole) = 0.0269\ T_M^{0.359} + 1.953x10^{-7}\ T_M^{1.903} \qquad (13)$$

Here it is assumed that all He atoms within a single bubble are in the same physical state, which was demonstrated experimentally by "hole-burning" of the resonance line [6]. Thus for each sample of unique age or He/M, the NMR data can be used to deduce the fraction of He atoms at each He density or molar volume v. The fraction of He that melts due to a small increase in molar volume ∂v (resulting from a small increase in temperature) is the change in the measured liquid fraction

$$F_{He}(v) \equiv \partial f_{liq}/\partial v. \qquad (14)$$

This $F_{He}(v)$ is the He atom distribution function; i.e., the fraction of He atoms with molar volume v in the interval v to v+dv.

Most of these He state measurements were made well below room temperature; thus it is necessary to correct the deduced v for the sample contraction occurring between room temperature and the measurement temperature. (Note that the bulk He contraction is greater than the metal contraction; and hence the bubble pressures drop with temperature even more than that predicted by the bulk He EOS. Thus no additional bubble enlargement will occur by loop punching during the low-temperature excursion. This would not be the case for experiments performed on aged material above room temperature, where one would expect non-reversible, additional loop punching effects to occur on the bubbles.) Correcting the He molar volume for each data point to room temperature using the thermal expansivity dL/L of Pd [30],

$$dV/V = 3\,dL/L$$
$$= -7.443\times10^{-3} + 5.611\times10^{-6}T + 9.878\times10^{-8}T^2 - 1.056\times10^{-10}T^3 \qquad (15)$$

results in the $f_{liq}(v)$ data plotted in Figure 4, for the four NMR samples of ages 0.5, 2, 4, 7 years. These curves give is the fraction of He atoms with atomic volume greater than v_a at room temperature.

For each sample, these data were least-squares fit to a linear function $f_{liq}(v_a)=A-Bv_a$ extending over the range $0\le f_{liq}\le 1$. The corresponding fit parameters are listed in the inset in Figure 4. Specific data points for which $f_{liq}=0$ or 1 were excluded for these fits since they do not necessarily define the melting transition. The best fit for the 4 year old sample, obtained taking into account increased scatter in the data points, deviates somewhat from the least-squares fit (dotted line). To avoid overweighting the extremum data for this sample, the solid line fit was obtained by averaging two linear fits, with and without the lowest $f_{liq}(v_a)$ data point. Little improvement in the overall data fits can be obtained using higher-order polynomials, particularly for the 2 year and 7 year samples where the data uncertainty is

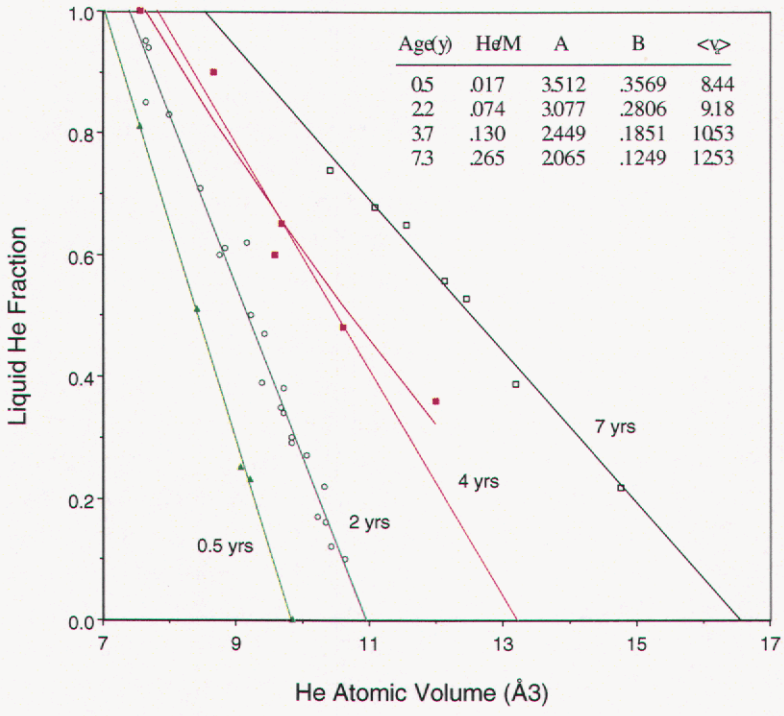

Figure 4. Fraction of ^{3}He atoms in the liquid state vs He atomic volume (at room temperature), determined from NMR T_1 data [5,6] on samples of 4 ages and the bulk He melting curve. Linear fits, A-Bv$_a$, are described by parameters A and B.

small. This is not true for plots of the same data as a function of temperature or He density, where quadratic and cubic polynomials become warranted.

The mean He atomic volume $\langle v_a \rangle$ at room temperature was calculated for each sample from the analytic fit. With the data plotted this way, this is the atomic volume at the point where the liquid fraction is half the total signal. Since the data are linear in v_a, from Eq. (14), the He atom distribution function $F_{He}(v_a)$ is independent of v_a for each sample. It has the value $F_{He}=B$ which varies inversely with the spread of v_a present within the sample. Also, it can be noted that the minimum He atomic volume deduced from these NMR data does not appear to be limited to 8.8 $Å^3$. In fact, the 0.5 year sample appears to have 20% or less (see below) of its helium still in the solid phase at room temperature, which requires a v_a=7.7 $Å^3$ or less. These are measurements on the He bubbles themselves and, unlike the swelling measurements, are not sensitive to volume changes produced by trapped clusters of dislocation loops and other defects created during the bubble growth.

These analytic fits to He melting data are converted from helium atom distributions $F_{He}(v_a)$ to bubble distributions F_b using the following expressions:

$$F_b(r) = (df_{liq}/dr) / N, \text{ normalized}$$
$$F_b(R) = (df_{liq}/dR) / N, \text{ normalized}, \qquad (16)$$

where (df_{liq}/dr) and (df_{liq}/dR) are obtained numerically using Eqs. (7), (8), and (10) to calculate v and N for a given r and He/M. The 1/N(r) factors are included to account for the number of He atoms within the bubble of radius r or spacing R. Dividing by N(r) converts the fraction of He atoms in bubbles with radius between r and r+dr to the fraction of bubbles with radius r in this interval. The functions $F_b(r)$ and $F_b(R)$ are then normalized by requiring each to equal unity when integrated over the full range of r or R, respectively.

The resulting bubble size and bubble spacing distribution functions are shown in Figures 5a and 5b. As expected, the mean bubble radius increases with age, in agreement with Figure 2a. Importantly, Figure 5b shows that the bubble spacing, and its distribution, is the same for each of the older samples. Although the 0.5 year sample appears to possess a significantly different spacing distribution, it is noted that these normalizations are correct provided no He is missed and the experimental data is over a high enough temperature range to melt the He in the smallest, highest-pressure bubbles. For the 0.5 year sample this requires temperatures above room temperature, the highest temperature used. As a result and due to the observation that NMR relaxation of solid He adjacent to the metal surface is modified by the surface [47], it is argued that a significant fraction (about half) of He atoms was missed for the 0.5 year sample. This caused the normalization process to increase the remaining part of the distribution by about a factor of two. If the curve for the 0.5 yr sample plotted in is reduced by one-half, it overlaps nicely with the other sample distributions. This uniqueness of the bubble spacing distribution provides strong support for both the absence of latent bubble nucleation and for the model formulation of the growth stage.

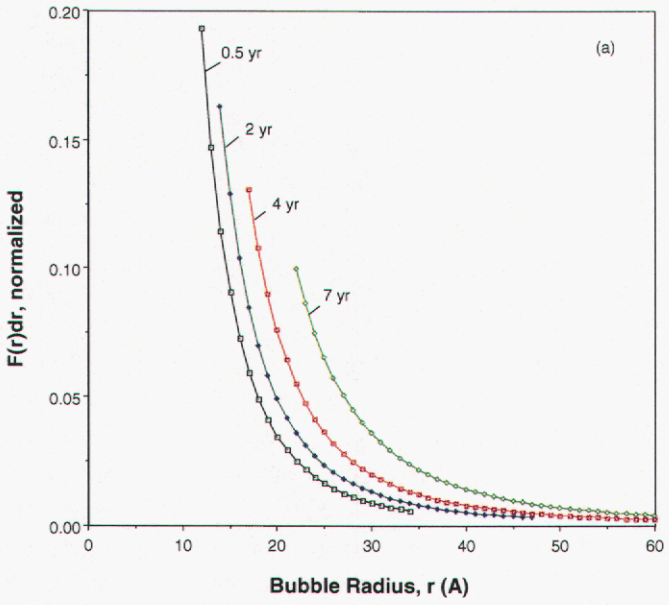

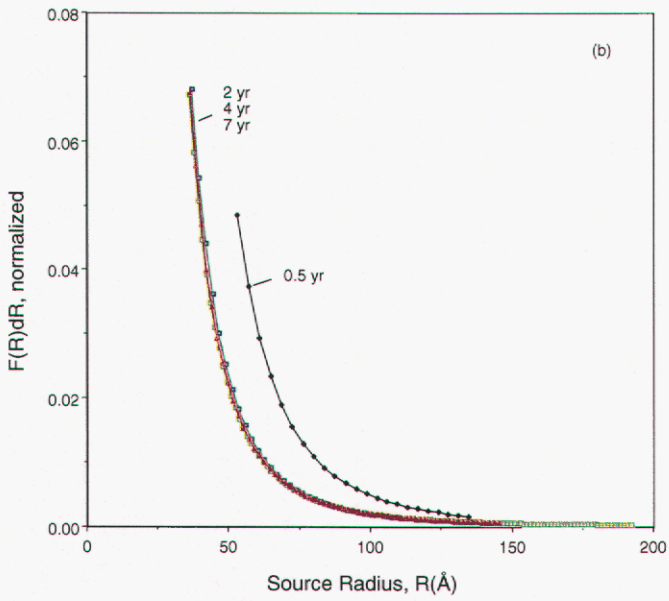

Figure 5. Bubble (a) size and (b) spacing distribution functions deduced from ^{3}He NMR T_1 data. The bubble radius increases with age but the spacing 2R is constant, verifying nucleation has stopped. Loss of data on bubbles smaller than r≈12Å produced incorrect normalization of $F_b(R)$ for the 0.5 yr sample.

The skewed shape of the spacing distribution can be attributed to the nucleation dynamics. Very early, bubbles are likely nucleated randomly with large spacings. As time progresses, additional bubbles are nucleated "in-between" with a probability which increases with the unoccupied volume between existing bubbles. As a result, larger spacings are converted into a greater number of smaller spacings, compressing the distribution toward smaller source radii R. However, since the mobile He concentration is reduced in the proximity of an existing bubble, very closely spaced bubbles are rare. Continued subdivision is terminated when the existing bubble surfaces provide a density of traps sufficient to reduce the mobile concentration, in accordance with Eq. (2). Thus, this shape is likely a consequence of this discreet nature of the nucleation process and the fact that the bubbles are immobile. A useful fit to this normalized distribution function is provided by the expression

$$F_b(R)_n = -.0069 + 1.560/R - 127.9/R^2 + 5341/R^3, \qquad (17)$$

where R(Å). Some additional bubble nucleation may occur later in life, beyond the current range of the NMR data. However, since at this point the mobile He concentration is low, it is likely that any such new bubbles will be nucleated at defects (e.g., dislocation loop clusters) created by the bubble growth process rather than by the self-trapping mechanism.

BUBBLE-BUBBLE INTERACTIONS

Thus far, bubble growth has been examined from the point of view of isolated bubbles. However, later in life their interactions should become important. The stress at a bubble's surface produced by a neighboring bubble can enhance the local shear and reduce the bubble pressure required for loop punching. In this non-uniform stress field, the loop-punching pressure becomes that needed to initiate a loop at the bubble's surface. Once this first metal atom exceeds the local potential barrier (b/2 displacement), it begins dropping into the next well and assists an adjacent atom in mounting its barrier, and so on, causing the loop to be sequentially formed around the bubble and finally freed from the bubble. Thus the point of loop initiation is near the location where the stress field produced by the neighboring bubble gives a maximum enhancement of the shear stress.

The radial and tangential stress components produced by an overpressure bubble at a distance u are $\sigma_r = -p(r/u)^3$ and $\sigma_t = (p/2)(r/u)^3$, respectively. These components give a shear stress at the bubble's surface of $\tau_{isol} = (1/2)(\sigma_t - \sigma_r) = 3p/4$. A simple superposition of these stress components finds that for a pair of identical bubbles separated by a distance 2s, the point of maximum shear on each bubble's surface is on the line adjoining their centers. At this point the shear is

$$\tau = (3p/4)\{1 + [\alpha/(2-\alpha)]^3\}, \qquad (18)$$

where $\alpha = r/s$. Since the stress drops slowly with small angles from this point around the bubble, this shear enhancement will exist at nearby locations consistent with loop punching directions (Burgers vectors). The bubble pressure is reduced by the interaction and becomes

$$p_{enh} = 2\gamma/r + (\mu b/r)/(1+\varepsilon), \qquad (19)$$

where $\varepsilon = [\alpha/(2-\alpha)]^3$ is the shear enhancement produced by the neighboring bubble. This enhancement factor and relative pressure are shown in Figure 6a. When extrapolated to the point where the two bubbles touch, the expression gives a loop-punching pressure one-half that of the isolated bubble.

At bubble spacings and radii where the shear enhancement becomes significant, an additional factor can come into play. Although the dislocation loops are punched in directions roughly orthogonal to the neighbor bubble, typically the bubble pair is not isolated. It is surrounded by additional bubbles, which can "block" the punching of full circular loops. This loop blocking is partial in that crescent-shaped loops are still able to pass the neighbor bubbles, as depicted by the inset in Figure 6b. This effect can be included to first order by excluding the fraction of punching space occluded by the array of nearest neighbor bubbles. For a regular fcc or hcp bubble geometry, the blocked areal fraction is

$$\beta_{hcp} = 12(\pi r^2)/[4\pi(2R)^2] = (3/4)\alpha^2. \qquad (20)$$

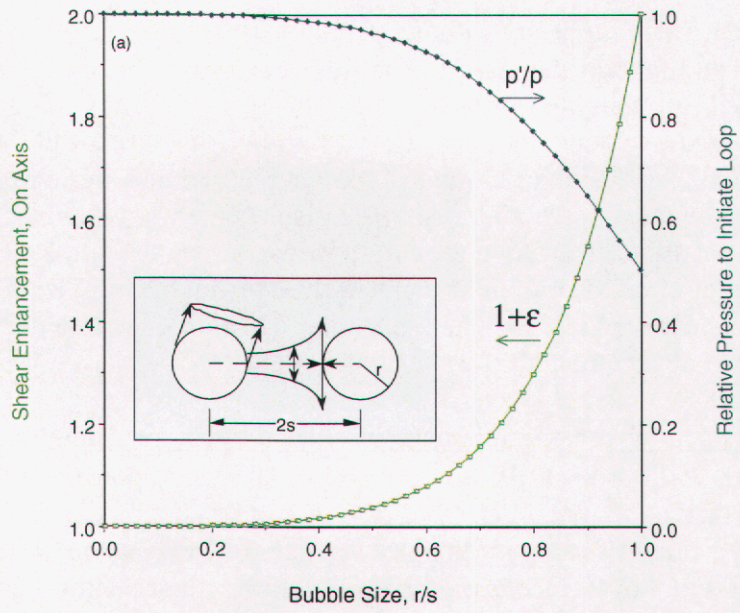

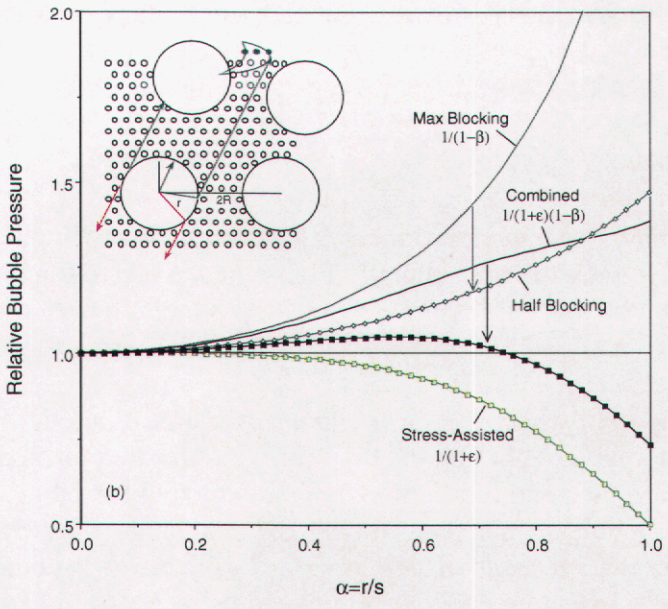

Figure 6. (a) Shear enhancement produced at bubble's surface by a neighboring bubble and bubble pressure required for loop punching. (b) Increases in the bubble pressure due to a partial blocking of loops by neighboring bubbles. For random bubble arrays, the blocking is less efficient, perhaps half that calculated using regular arrays.

With variable bubble packing, the average blocked areal fraction is approximately $\beta \approx f_p \alpha^2$, where f_p is the packing fraction discussed earlier. Assuming that the average punched loop area is reduced by this blocking factor raises the punching pressure for interacting bubbles from Eq. (19) to

$$p_{blocked} = 2\gamma/r + (\mu b/r)/\{(1+\varepsilon)(1-\beta)\}, \qquad (21)$$

for the combined interaction. Clearly the shear enhancement and loop blocking effects will at least partially cancel.

The factors $1/(1+\varepsilon)$ and $1/(1-\beta)$ are plotted in Figure 6b as a function of $\alpha=r/s$ for random packing. It is emphasized that loop blocking formulated in this average fashion must be considered an upper bound for random bubbles. In general, loops will be punched in the easiest direction, i.e., toward the largest open area consistent with the stress enhancement and Burgers vectors. For non-symmetric random bubble packing, use of this average blocking factor will overestimate the blocking by excluding the likely existence of compatible directions with open areas larger than this average. Thus the combined bubble interaction will fall below the curve labeled $1/\{(1+\varepsilon)(1-\beta)\}$. The dashed curve is shown as an example of the possible reduction. It shows the combined effect if the blocking is reduced from its maximum value by a factor of two. Since the loop blocking may be even less, it will be assumed negligible in comparison with the shear enhancement.

Bubble interactions can produce additional effects on bubble growth. It may be observed from Figure 6b that the shear enhancement at bubble A due to bubble B is larger for loop punching in the upper (blue) direction than it is for the lower (red) direction, since loop initiation occurs nearer the line connecting the two bubble centers. This can cause directed bubble growth, which in turn can lead to several significant effects. First, since the bubble surface facing a closely-spaced neighbor is always involved with the movement of metal atoms by loop punching in comparison with the opposite face, the two bubbles should preferentially grow toward each other more often than apart, tending toward bubble coalescence. Second, directed growth can cause bubble ordering along the Burgers vectors. This can be seen by examining likely growth directions for two adjacent bubbles with centers misaligned with respect to a Burgers vector. The bubble below the vector tends to grow upward and that above, downward. After becoming aligned along the Burgers vector, the neighbor bubble itself will begin blocking the punching of full loops when $\alpha=3^{1/2}/2$. Third, for two bubbles of different sizes, the effects are not symmetric. Small bubbles produce larger effects on neighboring large bubbles, than the reverse. Strong nearby bubble interactions may also produce local stress fields leading to stable bubbles of non-spherical shape. Clearly any non-isotropic growth can slowly modify the source volumes and bubble array geometry, deviating from the early growth assumption of fixed packing. These effects may become important late in life.

The center-to-center spacing between nearest neighbor bubbles 2s is important for calculations involving bubble interactions. It impacts bubble growth through the parameter $\alpha=r/s$. Here, the distance s has been used to differentiate it from R, the radius of the tritide source contributing He to the bubble's growth. It is argued that since loops are not punched

directly at close neighbors, the ejected material should not increase their spacing. These loops will more likely build up in the more open, lower-stress regions. In doing so, they can still contribute to the average bubble source volume, keeping R^3-r^3 roughly constant, while not increasing 2s. On the other hand, if directed growth is significant, the parameter 2s will decrease with age. For the calculations to follow, it is assumed that 2s remains fixed.

Interacting Bubbles in Palladium Tritide

Bubble pressures in $PdT_{0.67}$ computed using μ=33.6 GPa are shown in Figure 7. The solid curves in Figure 7a were calculated with Eq. (19), assuming random bubbles at densities of 2, 5, and $10x10^{17}$ bubbles/cm^3. The dashed curve for $5x10^{17}$ bubbles/cm^3 is included to show the weak dependence on bubble packing geometry. Since the bubble pressure appears more sensitive to n_B than does the swelling (Figure 3), it is interesting to compare these calculations with experimental pressures deduced from the average He atomic volumes v_a listed in Figure 4. Use of Eq. (12) gives average pressures described by the solid data points in Figures 7a and 7b. Here, the corresponding values of r/R and r were determined from He/M and v_a using Eq. (7). Figure 7a shows that bubble pressures calculated using $5x10^{17}$ bubbles/cm^3 produce the best fit to the NMR data. Increasing the shear modulus to the isotropic V-R average of G=45.2 GPa raises the calculated pressure, requiring a lower bubble density to fit the data. Conversely, the higher bubble density reported by Thiebaut *et al.* [39] would require a shear modulus even smaller than μ=33.6 GPa to fit the data.

Figure 7b shows that the pressure in initially isolated bubbles drops as 1/r, in accordance with Eq. (8). Later in life, stress produced by bubble interactions causes the pressure to drop faster than the isolated bubble case. Both the experimental bubble pressure and swelling, show no indication of a lower pressure limitation for larger bubbles proposed by Trinkaus and Wolfer [25]. Quite the opposite, the data point at the highest He/M (greatest r) indicates the bubble pressure may drop even faster than Eq. (19), the neighbor-enhanced stress rate. Use of the pressure expressions involving logarithmic factors [23, 27] gives pressures with lower values and slower change with r for larger bubbles, further deviating from the NMR data. On the other hand, one could argue that the NMR data point at highest He/M (largest r) may include the beginning effects of bubble linkage. Any such larger bubbles will skew the average bubble pressure toward lower pressure. As seen in Figure 5b, the spacing distribution for his sample has long tail to higher spacing, indicative of a small concentration of larger bubbles. However, since the distribution does not appear significantly affected in comparison with those at younger age, this tail apparently has little effect on the sample's average v_a or p.

Aging tritide pressure-composition-temperature (PCT) data provide another way of testing the bubble pressure dependence. The chemical potential of the hydride phase is modified by the net lattice tension produced by the high-pressure bubbles. The mean plateau pressure of the hydride shifts [48-49] from a bubble-free value of p_o to

$$p_{hy}=p_o\exp(-2\sigma_h v_{hy}/R_gT), \qquad (22)$$

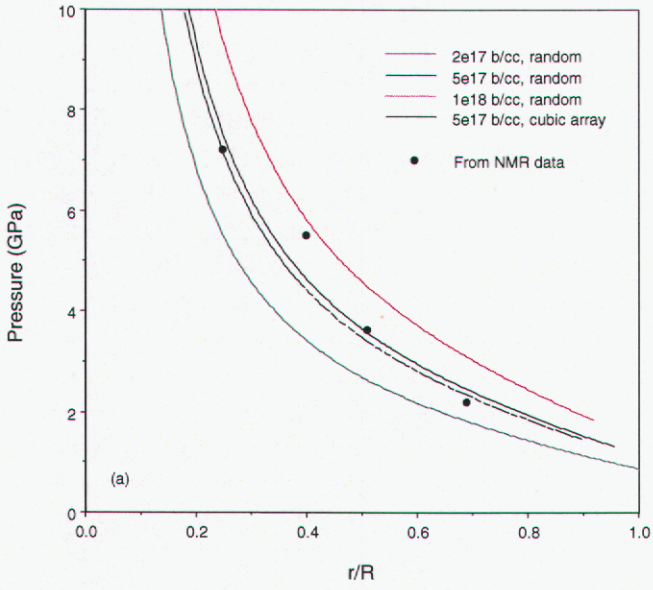

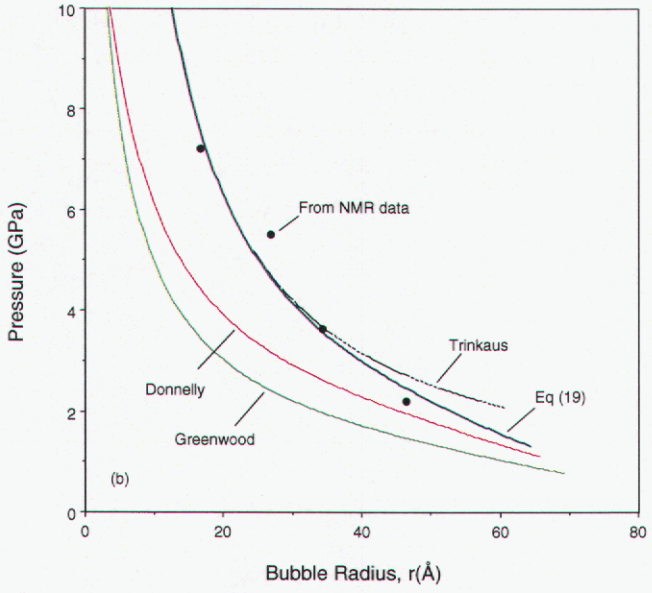

Figure 7. (a) Computed bubble pressure verses r/R and its dependence on bubble density, showing pressures computed with $5x10^{17}$ bubbles/cm^3 agree best with the NMR measurements. (b) Pressure change with r showing 1/r (Trinkaus) behavior at low r becomes more rapid at large r, in agreement with Eq. (19). The logarithmic expressions of Greenwood *et al.* [23] and Donnelly [27] do not fit the NMR data.

where σ_h=pB/(1-B) is the hydrostatic stress created by He bubbles at pressure p with a volume fraction B. Here v_{hy}=1.57 cc/mole is the partial molar volume of hydrogen in the hydride and R_g is the gas constant. For PdT with $5x10^{17}$ bubbles/cm^3, Eq. (22) gives the average plateau shift with age shown in Figure 8a. This shift is compared with Guthrie's measurements [48] for PdT with He/M=0.179 in Figure 8b. Guthrie found both the absorption and desorption curves depressed by the presence of bubbles. The model accurately predicts the average value of this depression, p_{hy}/p_o=0.57. It gives an average bubble pressure of <p>=4.15 GPa, which corresponds to an average He atomic volume of $<v_a>$=10.2 Å^3, which is not limited by the minimum value 8.8 Å^3. The model also predicts a weak temperature dependence, which is smaller than the scatter in the data.

The PCT comparison is complicated by the notion that the act of de-hydriding the sample during the desorption measurement causes lattice shrinkage, forcing the punching of additional loops. When re-hydrided during absorption, the lattice then expands lowering the bubble pressures and changing the PCT shift. Since adsorption occurs from the metallic state, it is subject to the higher bubble pressures, whereas desorption occurs from the hydride state and (except for the first cycle) lower bubble pressures. The magnitude of this effect can be estimated by considering the PCT shift with volume change. Palladium hydride contracts 11% with de-hydriding, increasing v_a for re-hydrided material from 10.2 to 11.3 Å^3 and, according to Eq. (11), giving a 5% lower average bubble pressure. However, the 11% increase in B more than compensates for this pressure drop, resulting in a net 6% increase in σ_h. This increases the depression of the average plateau to $p_{hy}/p_o \approx 0.56$, a negligible change in the PCT. However, the increase in v_a is observable in its effect on the ^{3}He NMR. Cowgill [50] found the ^{3}He T_1 relaxation time for re-hydrided, 7 year old $PdT_{.65}$ to be 7 times longer than for H-exchanged material, consistent with an increased He mobility within the bubbles. The magnitude of this change was interpreted to indicate the bubbles indeed expand 11% with the β–α–β phase cycle.

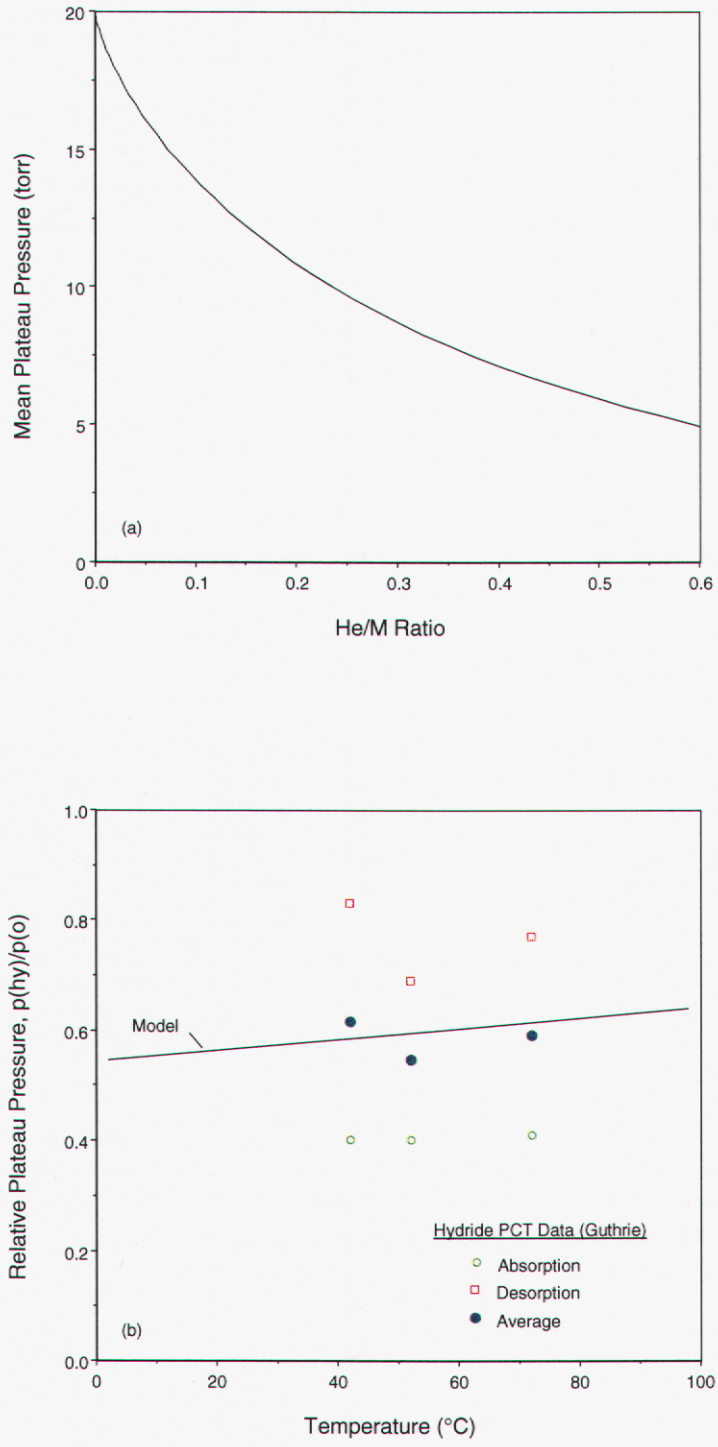

Figure 8. (a) Mean Pd hydride plateau pressure drop at 300 K, computed for $5x10^{17}$ bubbles/cm^3. (b) Relative plateau pressure for PdT with .179 He/M showing comparison with data of Guthrie [48].

RAPID HELIUM RELEASE

As the bubbles grow, the metal ligament between them becomes shorter. Increased stress in this ligament region can lead to inter-bubble fracture and, eventually, helium release. Evans [51] generated a blistering criterion for ion-implanted materials based on the average stress on this ligament. His criterion can be extended to our 3-dimensional bubble arrays. Consider a plane through three adjacent bubbles within the array, as shown by the inset in Figure 9a. The force tending to separate the metal normal to this plane is the bubble pressure times the bubble area fraction. Similarly, the cohesive force holding the plane together is the metal's theoretical fracture strength times the metal area fraction. Balancing these two forces gives Evans' pressure for inter-bubble fracture,

$$p_{IBF} = 2\gamma/r + \sigma_F [(\pi r^2 n_b^{2/3})^{-1} - 1], \qquad (23)$$

where σ_F is the theoretical fracture strength and the factor in square brackets is simply the ratio of the metal area to the bubble area. At large r, this factor decreases as $1/r^2$, dropping the fracture pressure below the loop punching pressure which decreases roughly as 1/r.

Inter-bubble Fracture in Palladium Tritide

The transition from dislocation loop punching to inter-bubble fracture in PdT is shown by the intersection of the two pressure curves in Figure 9a. Here the loop punching pressure was calculated from Eq. (19) using μ=33.6 GPa and random bubbles at a density of 5×10^{17} bubbles/cm^3. The fracture pressure was calculated using Eq. (23) with the fracture strength $\sigma_F=(4/3)\tau_{max}$. The critical concentration at ligament fracture is found to be 0.54 He/M. Using $\sigma_F=G/4\pi$ produces the slightly higher critical concentration of 0.59 He/M. At either critical He/M, α is greater than $\sqrt{3}/2$, the point where the neighbor bubble begins to produce some loop blocking. However, it can be shown that this blocking still remains small and produces a negligible effect on the bubble pressure or the critical He/M.

Both pressure curves in Figure 9a shift with bubble density n_B, causing a shift in the critical He/M. Figure 9b gives the locus of the fracture points for bubble densities from 10^{16} to 10^{19} bubbles/cm^3. The model shows that bubble densities near the 5×10^{17} bubbles/cm^3 should achieve the highest He/M ratio prior to inter-bubble fracture. Bubble densities either higher or lower than this value will reduce the critical He/M concentration.

For random bubble packing, there exists a distribution in the nearest neighbor bubble spacing. (See Figure 5b, for example.) This distribution causes some bubbles to "link-up" earlier than others. Generation of an inter-connected linkage to the material surface will produce release of the He contained within these linked-bubbles. Once this network becomes fully established, the material will be in a state of rapid He release in that new He atoms will be released at the generation rate. The onset of this rapid release state should be describable using percolative or effective medium approaches. In this paper, it will be assumed that rapid release occurs when bubbles at the mean bubble density experience inter-bubble

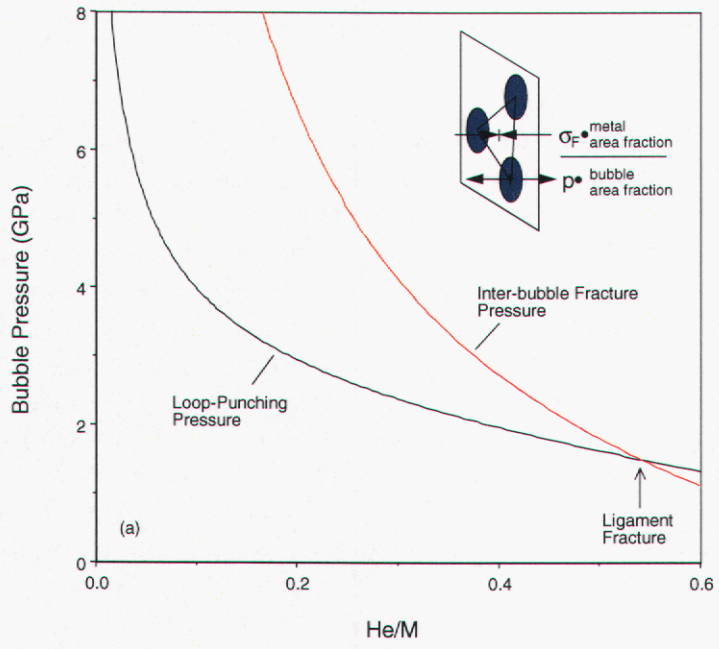

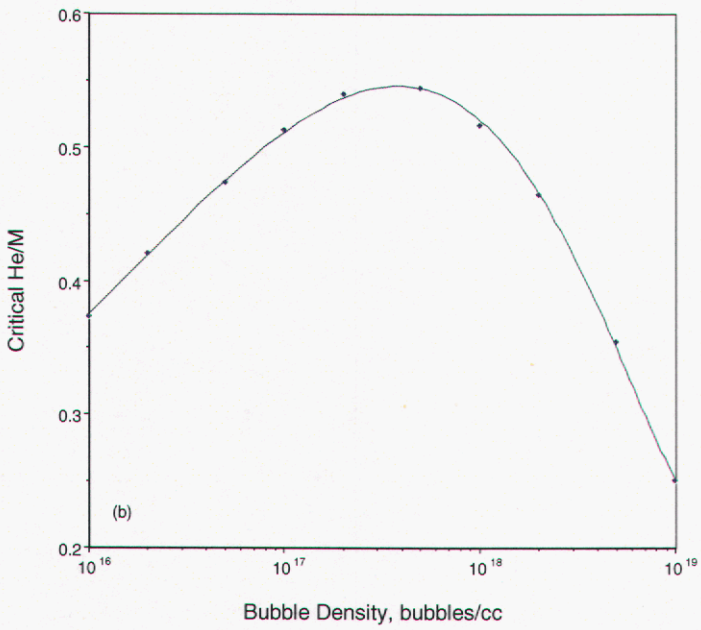

Figure 9. (a) Inter-bubble ligament fracture for PdT at 300 K, computed for $5x10^{17}$ bubbles/cm^3 using Evans' expression for the average ligament stress and $\sigma_F=(4/3)\tau_{max}$. (b) Dependence of this critical He/M on bubble density.

fracture. Thus the model predicts rapid He release from bulk PdT will occur at 0.54 He/M. The onset of rapid He release from large particle powders has been reported to occur between 0.50-.55 He/M [52-53], in good agreement with this value. Since this material had a particle size 1000 times the bubble spacing, a well-developed fracture network would be expected to be required for rapid release.

Rapid release should occur somewhat sooner for small particle powders. Within them, small inter-connected bubble clusters have a higher probability of intersecting the surface. An estimate of the fractional He release for small particle powders or films can be made by treating each part of the distribution separately and superimposing the linkages developed at each He/M. The distribution shown in Figure 5 has bubble spacings varying between 150 and 30 Å, corresponding to bubble densities of $4.5\text{x}10^{16} < n_B < 5.7\text{x}10^{18}$ bubbles/cm^3. From Figure 9b, this higher bubble density begins inter-bubble fracture around 0.35 He/M, while the lower density limit begins at about 0.47 He/M. Yet some inter-bubble ligaments remain intact until He/M=0.54. Thus for small powder particles, helium should begin releasing from linked bubbles at a slow rate around 0.35 He/M and then increase until it reaches the generation rate at 0.54 He/M. The release rate becomes a maximum when He in the bulk of the distribution is intercepted. Although the F(R) distribution peaks at low R, these are small bubbles, which contain little helium. The release becomes most rapid at the point where NF(R) or $R^3F(R)$ is a maximum. Using the fit to the distribution, Eq. (17), it is found that $R^3F(R)$ is maximized around R≈81 Å, or $n_B \approx 3\text{x}10^{17}$ bubbles/cm^2. This occurs at the peak of the curve in Figure 9b. That is, the release rate continues to increase until all parts of the bubble distribution have undergone inter-bubble fracture.

EARLY HELIUM RELEASE AND THE RELEASE SPECTRUM

Material surfaces or interfaces can reduce the mobile helium concentration by providing escape pathways or He atom sinks. Bubble nucleation is reduced in the proximity of these sinks. The bubble concentration profile in the vicinity of a surface can be modeled by adding a diffusive term to equation (2), giving

$$dc_1/dt = -D\, d^2c_1/dx^2 + g - 2p_1s_1c_1^2 + 2q_2c_2 - p_1s_2c_1c_2 - p_1s_Bc_1c_B, \qquad (24)$$

and imposing the boundary condition c(x,t)=0 for all t.

Early Release from Palladium Tritide

Numerically integrating the coupled Eqs. (24), (3), and (4) with the same diffusion and trapping parameters used above generates the mobile helium c_1 and bubble c_B profiles shown in Figure 10. After an initial transient where the spatial profiles are being established, their shapes remain fairly constant, while the magnitude of c_1 drops slowly with the increase in bubble surface area. The apparent decrease in bubble density near the sink has been described as a bubble denuded zone. Its thickness is about 1-2 bubble spacings, in agreement with that used by Forman and Singh [54]. From Figure 10, it appears this region is not totally denuded but rather possesses a "significantly depressed" bubble density. However, since its thickness is of the order of the bubble spacing, it appears denuded in TEM cross-section.

Denuded zones in contact with the external surface contribute the Early Release Fraction (ERF), defined here as the ratio of the rate of instantaneous helium release to the rate of helium generation within the material. Reduced trapping allows He atoms to escape from these regions throughout life. A measure of the escape thickness or escape length can be obtained from the calculated flux through the surface of a film on an impenetrable substrate. The release spectrum calculated for a 1 micron film is shown in Figure 11. There is an initial drop as bubbles are nucleated and grow sufficiently to prevent the escape of He generated deeper within the material. With time, the release begins to increase as the few bubbles near the surface "breach" the surface and release their helium. The calculation shown here assumes isotropic bubble growth and uses the breach condition r=x; that is, breach occurs when the bubble radius equals the depth to the bubble's center. This condition precludes potential motion of the surface due to the accumulation of dislocation loops. The discrete mesh size (Δx=4 Å) used for the calculation results in the artificial, stepped behavior caused by the breaching of successive layers.

The ERF is greater for thin films or small particle powders. The results from Figure 11 can be scaled with surface-to-volume ratio (S/V) for other film thicknesses, two-sided foils, powder particles or film grains with open (releasing) grain boundaries. For example, for spherical powder particles 1 micron in diameter, S/V=3/r and the ERF should be increased by factor of six.

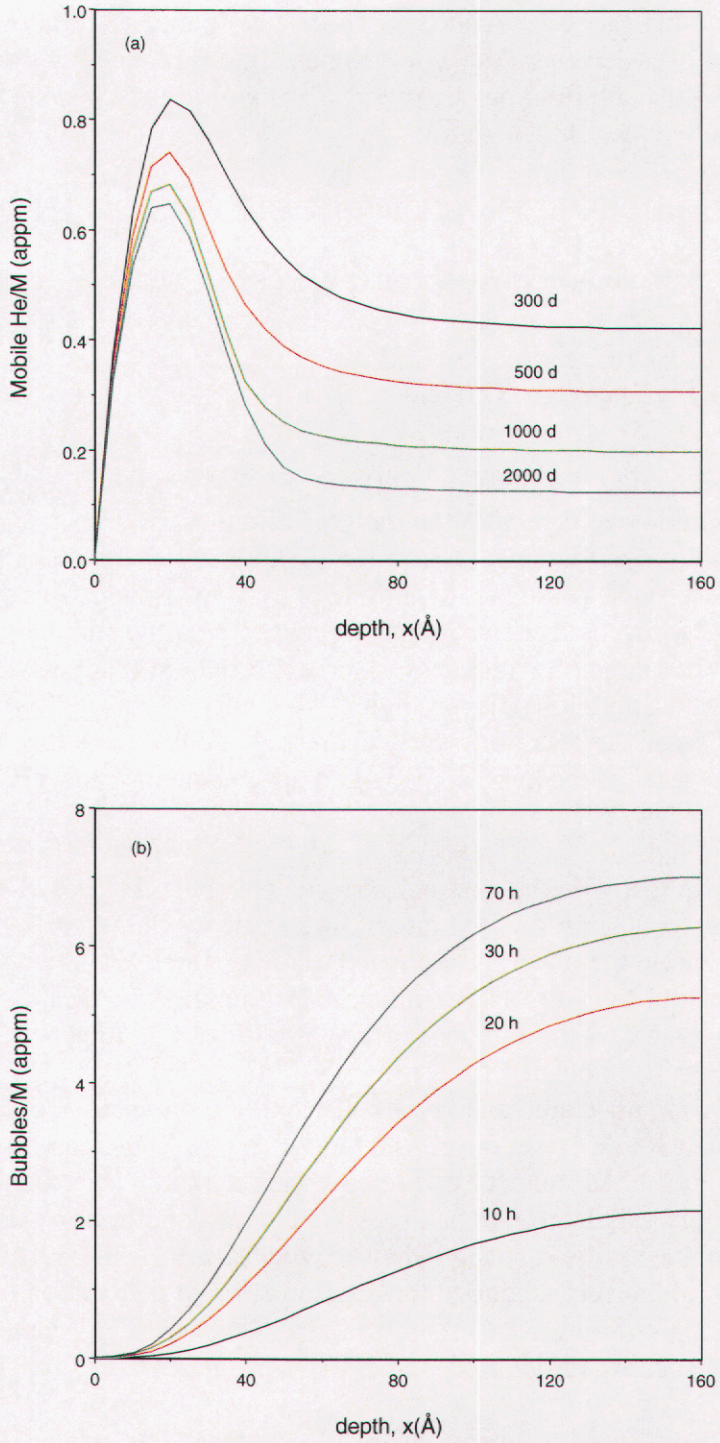

Figure 10. Calculated depth profiles in $PdT_{0.65}$ of (a) mobile He, c_1, showing persistent, high near-surface concentration and (b) bubble concentration, c_B, showing near-surface denuded zone.

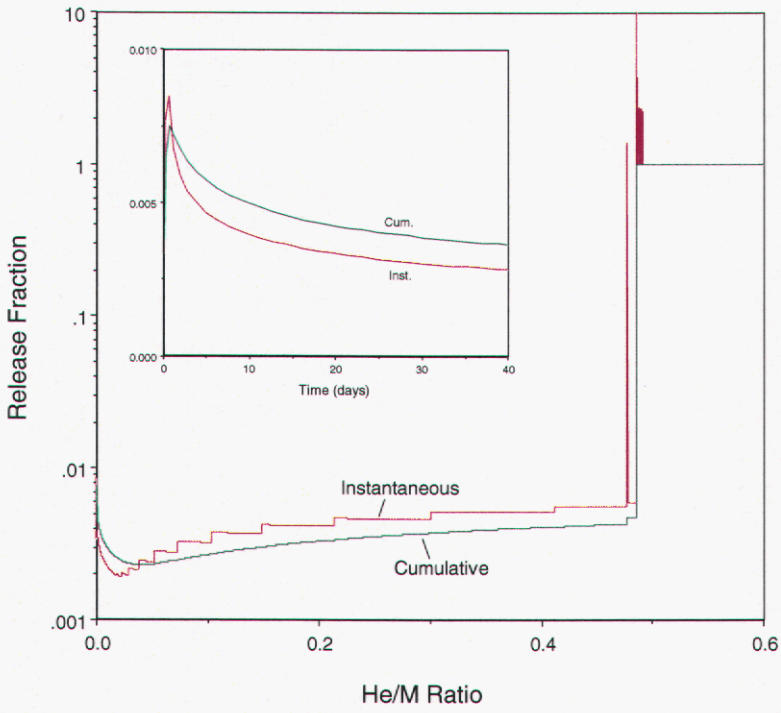

Figure 11. Computed He release with age for a 1 μm thick $PdT_{0.65}$ film on an impenetrable substrate. An initial drop occurs as bubbles are nucleated, followed by a slow rise as bubbles breach the surface, then rapid release due to inter-bubble fracture. The instantaneous release, averaged over 1 hr intervals, exceeds the generation rate at the onset of rapid release.

The He escape length λ_{esc} can be defined as the equivalent thickness of a surface layer releasing its He at the generation rate on top of material with no early release. With this definition, the ERF is the ratio of the escape length to the film thickness. For the example of Figure 11, this escape length has a minimum value of λ_{esc}=20 Å around 0.02 He/M, increasing to λ_{esc}=50 Å just before rapid release. It can be compared with the escape depth for a film with a fixed, uniform concentration of traps, which can be evaluated analytically. Carslaw and Jeager [55] examined this problem as the temperature profile of a slab with uniform internal heat generation. They showed the temperature profile has an inverted parabolic shape, increasing from the surface temperature to a maximum midway through the slab. Here, the equivalent midway depth is $(2Dc_M/g)^{1/2}$, where c_M is the steady-state mobile He concentration at points distant from the surface. At steady-state, $g-pc_Ms_Bc_B=0$ or $c_M=gb^2/12Ds_Bc_B$. Equating the integral over this profile to $1-\lambda_{fixed}$ (for the single-sided film) gives the equivalent thickness for a $c_M=0$ layer: $\lambda_{fixed}=(b/3)/(6s_Bc_B)^{1/2}$. Choosing s_B=12 and

$c_B=8x10^{-6}$ bubbles/M yields $\lambda_{fixed}=40$ Å, midway between the above two values for λ_{esc}. Alternatively, the minimum escape length of $\lambda_{esc}=20$ Å is comparable to that produced by a uniform density of bubbles with about 50 trapping sites per bubble, which corresponds to a bubble diameter of about 6.6 Å. Since in the present case, the bubbles are somewhat denuded throughout this region, larger bubbles would be required to produce the same trapping effect, in accordance with the bubble sizes calculated in Figure 2.

SUMMARY AND CONCLUSIONS

An evolutionary model of helium nano-bubble nucleation, growth and He release for aging metal tritides has been developed which is successful in explaining major features of the experimental database. It is primarily a compilation of individual models from the literature describing each physical process. Bubble nucleation is modeled according to Wilson *et al.* as self-trapping of He atoms which diffuse into adjacent interstitial sites. Nucleation is shown to occur during the first few days following tritium introduction into the metal and is sensitive to the He diffusivity and pairing energy. Use of the pairing energies calculated by Wilson *et al.* requires a helium diffusivity of 0.3×10^{-16} cm^2/s at 300 K to generate the TEM-observed average bubble density of 5×10^{17} bubbles/cm^3 reported by Thomas and Mintz. Early bubble growth by dislocation loop punching with Trinkhaus' 1/radius bubble pressure dependence along with this bubble density produces bubble pressures (and He atomic volumes) in good agreement with those determined from swelling data, NMR measurements, and metal tritide PCT shifts. An unrealistically low shear modulus for the PdT system would be required to accommodate the 10x greater bubble density reported by Thiebaut *et al.* New interpretation of the ^3He NMR data of Abell *et al.* for 0.5 year old PdT shows the atomic volume of helium within it's very small bubbles is less than the minimum value of 8.8 $Å^3$ calculated by Schober *et al.* The NMR behavior for this sample is consistent with a significant fraction of the helium existing in the solid state at room temperature.

The nucleation model not only accounts for the observed bubble density. The nucleation dynamics qualitatively explain the shape of the bubble spacing distribution obtained from NMR data. When this distribution is evaluated separately for datasets from four samples up to 7 years old, it is found to remain fixed with age, providing a sensitive validation of the growth formulation and indicating that significant further bubble nucleation does not occur. This observation validates the model's separation of the nucleation and growth stages. Later in life neighboring bubble interactions are proposed to first lower the loop punching pressure through cooperative stress effects then perhaps raise the pressure by partial blocking of loops. This behavior is consistent with the limited experimental database, but needs further testing.

Early helium release is shown to result from He generated within the escape depth of surfaces and surface-connected porosity. For aging $PdT_{0.65}$, the effective escape depth is calculated to be only 20-50 Å, depending on the age of the material. This is about half the thickness of the bubble-denuded zone apparent from the calculated bubble depth profile. Rapid helium release is modeled as inter-bubble fracture using Evans' average ligament stress criterion. Good agreement is found between the predicted onset of fracture at 0.54 He/M and the critical He/M for rapid He release reported for bulk PdT by Abell *et al.* and Emig *et al.* This critical concentration is shown to depend on the mean bubble density and should have its largest value around 5×10^{17} bubbles/cm^3. Knowledge of the bubble spacing distribution is important for predicting the fractional bubble linkage at lower He/M. An examination of how inter-bubble fracture varies over the spacing distribution shows that the

critical He/M will be lower for thin films and small particle material. For the PdT distribution found here, the critical concentration can be as low as 0.35 He/M, depending on the degree of linkage needed for the interconnected bubble network to traverse the particle. It is concluded that bubble evolution, the early release fraction, and the onset of rapid release are all controlled by the nucleated bubble spacing distribution and its variation near surfaces.

Further testing and validation of the model will require additional measurements on the bubbles themselves. To date, NMR and TEM appear to yield the most useful data. NMR provides more sensitive testing of bubble growth physics than does the integral swelling or hydride PCT behaviors. It can measure the important bubble spacing distribution and characterize how intrinsic material defects change this distribution, both of which affect bubble growth and He release. For data from aged material to be useful, these effects must be known. NMR gives information on all parts of this distribution, allowing study of effects on small bubbles to be distinguished from those on large. Additional NMR and TEM studies are particularly needed for further examination of the mechanism responsible for He release. These techniques should be capable of providing details on the physics of inter-bubble fracture; through, for example, changes in bubble pressures and bubble shapes just prior to bubble linkage and rapid release.

REFERENCES

1. J.M. Mintz and G.J. Thomas, 1983, J. Nucl. Mater. 116:336.
2. R. Lasser and T. Schober, 1984, J. Nucl. Mater. 120:137.
3. R. Lasser, T. Schober, and H. Trinkaus, 1986, J. Nucl. Mater. 141-3:453.
4. A. Attalla and R.C. Bowman, 1977, Phys. Rev. B 16:1828.
5. G.C. Abell and A. Attalla, 1987, Phys. Rev. Lett. 59:995; and 1988, Fusion Tech. 14:643.
6. G.C. Abell and D.F. Cowgill, 1991, Phys. Rev. B 44:4178.
7. M.I. Baskes, C.L. Bisson, and W.D. Wilson, 1981, Phys. Rev. B 24:5616.
8. M.I. Baskes and W.D. Wilson, 1983, Phys. Rev. B 27:2210.
9. W.G. Wolfer, 1989, Phil. Mag. A 58:285 and A 59:87.
10. M.I. Baskes, W.A. Swansiger, and G.J. Thomas, 1979, J. Appl Phys 50:6942.
11. R. Bastasz and G.J. Thomas, 1981, J. Appl. Phys. 52:6426.
12. M. Deicher, G. Grubel, E. Recknagel, W. Reiner, and T. Wichert, 1985, Phys. Rev. Letters 55:726.
13. H.K. Birnbaum and C.G. Chen, 1979, J. Nucl. Mater. 79:128.
14. M.I. Baskes, M.S. Daw, and W.D. Wilson, 1983, Calculations of Hydrogen and Helium in Metals, Advances in the Mechanics and Physics of Surfaces II, edited by T.E. Fischer and R.M. Latanision, Harwood Acad. Pub., New York.
15. D.F. Cowgill, to be published.
16. P. Jung, H. Trinkaus, and R. Vassen, 1991, J. Nucl. Mater. 183:1.
17. J. Amano and D.N. Seidman, 1984, J. Appl. Phys. 56:983.
18. W. Jager, R. Lasser, T. Schober, and G.J. Thomas, 1983, Radiat. Eff. 78:165.
19. W. Jager, R. Lasser, T. Schober, and G.J. Thomas, 1984, J. Nucl. Mater. 122-3:571.
20. K. Farrell and T. Schober, 1989, J. Nucl. Mater. 168:171.
21. D.A. Macinnes and P.W. Winter, 1983, J. Nucl. Mater. 114:7.
22. M.F. Wehner and W.G. Wolfer, 1986, J. Statistical Phys. 42:509.
23. A.J.E. Foreman, G.W. Greenwood, and D.E. Rimmer, 1959, J. Nucl. Mater. 4:305.
24. H. Trinkaus, 1983, Radiat. Eff. 78:189.
25. H. Trinkaus and W.G. Wolfer, J. Nucl. Mater. 122-3 (1984) 552.
26. B.B. Glasgow, H. Trinkaus, M.F. Wehner, and W.G. Wolfer, 1984, J. Nucl. Mater 122-3:565.
27. S.E. Donnelly, 1985, Radiat. Eff. 90:1.
28. J.C. Bronson, D.H. Liebenberg, and R.L. Mills, 1980, Phys. Rev. B 21:5137.
29. R.C. Weast, editor, 1984, CRC Handbook of Chemistry and Physics, 65:F-24, CRC Press, Boca Raton FL.
30. Y.S. Touloukian, editor, 1975, Thermophysical Properties of Matter, 12:248, Plenum, New York.
31. R.G. Leisure and L.A. Nytren, 1988, Phys. Rev. B 37:6482.
32. B.M. Geerken, R. Griessen, and L.M. Huisman, 1982, Phys. Rev. B 26:1637.
33. J. Rice, 1992, J. Mech. Phys. Solids 40:239.
34. C. Krenn, Lawrence Livermore National Laboratories. [private communication]
35. W.G. Wolfer, 1990, Elastic Properties of Aged Palladium Tritides, Technical Report SAND90-8253, Sandia National Laboratories.

36. O. Blaschko, D. Leroy, B. Limacher, C. Maier, V. Paul-Boncour, A. Percheron-Guegan, C. Tailland, and S. Thiebaut, 1998, Phys. Rev. B 57:10379.
37. S.E. Guthrie, 1989, Sandia National Laboratories, Livermore, CA. [unpublished data]
38. D.S. West, 1984-85, EG&G Mound Applied Technologies, Miamisburg, OH. [unpublished data]
39. B. Decamps, B Limacher, J.M. Penisson, A. Percheron Guegan, and S. Thiebaut, 2000, J. Nucl. Mater. 277:217.
40. D.H. Morse, A.E. Pontau, and K.L. Wilson, Sandia National Laboratories. [unpublished data, private communication]
41. C. Dieker, J. Golczewski, R. Lasser, T. Schober, and H. Trinkaus, 1985, Phys. Rev. B 31:7109.
42. C. Dieker, R. Lasser, T. Schober, and H. Trinkaus, 1987, J. Less Comm. Metals 131:293.
43. C. Dieker, R. Lasser, T. Schober, and H. Trinkaus, 1989, Phys. Rev. B 40:1277.
44. T. Schober and H. Trinkaus, 1991, J. Appl. Phys. 70:729.
45. N. Bloembergen, 1961, Nuclear Magnetic Relaxation, Benjamin, 92.
46. A.K. McMahan, M. Ross, and D.A. Young, 1981, Phys. Rev. B 24:5119.
47. R.A. Guyer, R.C. Richardson, and L.I. Zane, 1971, Revs. Mod. Phys. 13:532.
48. S.E. Guthrie and W.G. Wolfer, Sept. 22-26, 2002, How Helium Affects the Thermodynamics of the Palladium-Tritium System, International Conf. on Hydrogen Effects, Jackson Lake, WY.
49. S.E. Guthrie, 1990, Helium Effects on Palladium Hydride Equilibrium Properties, Technical Report SAND90-8233, Sandia National Laboratories.
50. D.F. Cowgill, 2001, Swelling of Aged PdTx During Hydride Phase Cycling, Technical Report SAND2001-8360, Sandia National Laboratories.
51. J.H. Evans, 1977-78, J. Nucl. Mater. 68:129 and 76-7:228.
52. G.C. Abell, R.C. Bowman Jr., L.K. Matson, B.M. Oliver, and R.H. Steinmeyer, 1990, Phys. Rev. B 41:1220.
53. L.D. Christensen, P.R. Coronado, J.A. Emig, R.G. Garza, and P.C. Souers, 1992, J. Nucl. Mater. 187:209.
54. A.J.E. Forman and B.N. Singh, 1985, J. Nucl. Mater. 133-4:451.
55. H.S. Carslaw and J.C. Jaeger, 1959, Conduction of Heat in Solids, 2nd Ed., Oxford, p 130.

Distribution

1 Gene Caveness, 773-42A
WSRS
PO Box 616
Aiken, SC 29808

1 Paul Cloessner, 773-A
WSRS
PO Box 616
Aiken, SC 29808

1 Burt Davis, ESA-GTS
Los Alamos Natl. Lab
P.O. Box 1663, G780
Los Alamos, NM 87545

1 Dennis Fish, 773-A
WSRS
PO Box 616
Aiken, SC 29808

1 David Gelles
Pacific Northwest Natl. Lab
P.O. Box 999 / P8-15
Richland, WA 99352

1 Kevin Honnell, ESA-GTS
Los Alamos Natl. Lab
P.O. Box 1663, C934
Los Alamos, NM 87545

1 Ken Keeler, ESA-GTS
Los Alamos Natl. Lab
P.O. Box 1663, C934
Los Alamos, NM 87545

1 Christopher Krenn
Lawrence Livermore Natl. Lab
P.O. Box 808, MC0470A
Livermore, CA 94551-0808

1 David Lohmeier, ESA-GTS
Los Alamos Natl. Lab
P.O. Box 1663, G780
Los Alamos, NM 87545

1 Brad Meyer, ESA-GTS
Los Alamos Natl. Lab
P.O. Box 1663, C934
Los Alamos, NM 87545

1 James Peery, ESA-GTS
Los Alamos Natl. Lab
P.O. Box 1663, G780
Los Alamos, NM 87545

1 Adam Schwartz
Lawrence Livermore Natl. Lab
P.O. Box 808, MC0470A
Livermore, CA 94551-0808

1 Kris Winer
Lawrence Livermore Natl. Lab
P.O. Box 808, MC0470A
Livermore, CA 94551-0808

1 Wilhelm Wolfer
Lawrence Livermore Natl. Lab
P.O. Box 808, MC0470A
Livermore, CA 94551-0808

1 Steven Wyrick, 773-A
WSRS
PO Box 616
Aiken, SC 29808

1	MS	0316	John Aidun, 9235	1	MS	9108	Robert Monson, 8243
1		0335	Carla Busick, 2564	1		9108	Tony Lajeunesse, 8243
1		0335	Clark Snow, 2564	1		9108	Carl Pretzel, 8243
1		0427	Jim Harrison, 2113	1		9108	Steve Robinson, 8243
1		0516	Robert Spulak, 2565	1		9108	G. Cook Story, 8243
1		0521	Frank Bacon, 2503	1		9108	Mike Hardwick, 8201
1		0824	Jaime Moya, 9130	1		9161	Walter Bauer, 8770
1		0835	Mike McGlaun, 9140	1		9161	Tony Chen, 8763
1		0871	Len Beavis, 14406	1		9161	J. Zimmerman, 8763
1		0871	James Browning, 14406	1		9161	Patrick Klein, 8763
1		0886	Paul Kotula, 1822	1		9202	Rena Zurn, 8418
1		0889	Dick Salzbrenner, 1835	1		9402	Dean Buchenauer, 8772
1		1056	Barney Doyle, 1112	1		9402	Chuck Cadden, 8772
1		1146	Pat Griffin, 6423	1		9402	Rion Causey, 8772
1		1146	Philip Cooper, 6423	10		9402	Don Cowgill, 8772
1		1411	Jeff Hoyt, 1834	1		9402	Kristin Hertz, 8772
1		1411	Stephen Foiles, 1834	1		9402	Brian Somerday, 8772
1		9004	Rick Stulen, 8100	1		9403	James Wang, 8773
1		9005	Ed Cull, 8240	1		9403	Arlyn Antolak, 8773
1		9007	Doug Henson, 8240	1		9403	Eric Mazjoub, 8773
1		9007	Brian Damkroger, 8210	1		9403	Dan Morse, 8773
1		9011	Chuck Oien, 9903	1		9405	Jill Hruby, 8700
1		9034	Russ Miller, 8221	1		9405	Ken Wilson, 8770
1		9052	Steve Rice, 8361				

3	MS	9018	Central Technical Files, 8945-1
1		0899	Technical Library, 9616
1		9021	Classification Office, 8511 for Technical Library, MS 0899, 9616 DOE/OSTI via URL